Modeling and Simulations of Retina-Like Three-Dimensional Computational Ghost Imaging
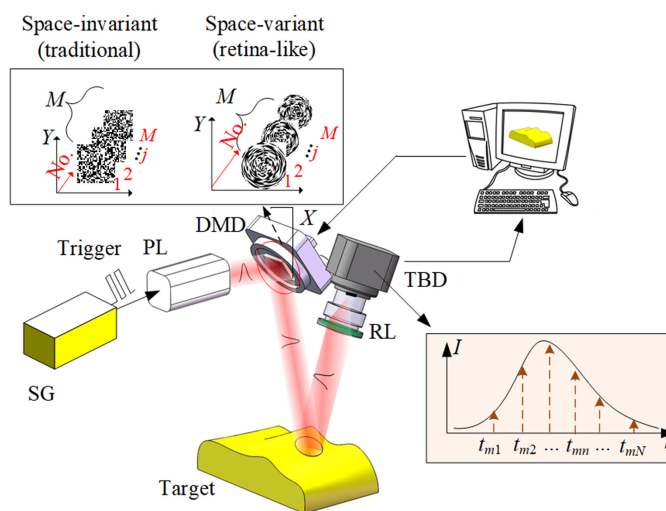
Kaiyu Zhang
Jie Cao
Qun Hao
Fanghua Zhang
Yongchao Feng
Yang Cheng

Modeling and Simulations of Retina-Like Three-Dimensional Computational Ghost Imaging

Kaiyu Zhang [ID],[1] **Jie Cao** [ID],[1,3] **Qun Hao,**[1,2] **Fanghua Zhang,**[1] **Yongchao Feng,**[1] **and Yang Cheng**[1]

[1]School of Optics and Photonics, Beijing Institute of Technology, Key Laboratory of Biomimetic Robots and Systems, Ministry of Education, Beijing 100081, China
[2]Graduate School at Shenzhen, Tsinghua University, Shenzhen 518055, China
[3]NUS Suzhou Research Institute (NUSRI), Suzhou Industrial Park, Suzhou 215123, China

Abstract: A retina-like 3-D (three-dimensional) computational ghost imaging (R-3DCGI) is proposed to obtain high resolution while maintaining high imaging efficiency. R-3DCGI models are developed, and corresponding simulations are conducted to verify and evaluate the accuracy and features of the R-3DCGI. Results show that the models obtain rotation and scaling invariances and compress redundant information, thereby improving imaging efficiency over the traditional computational ghost imaging. The relationships between parameters of the retina-like models and signal–noise ratio are discussed to optimize the retina-like structures in various applications.

Index Terms: Imaging systems, computational imaging, image reconstruction techniques.

1. Introduction

Ghost imaging (GI) provides target information by using a single bucket detector and a set of random patterns, which are produced by pseudo-thermal or thermal light source [1]. To simplify the structure of GI, a spatial light modulator or digital micromirror device (DMD) is used to construct computational GI (CGI) [2]. GI has been widely used in 2D and 3D imaging [3], [4], biomedical engineering [5], and secret communication [6] given the advantages of high sensitivity in detection [7], lensless [8], and anti-turbulence atmosphere [9].

The trade-off between the resolution and imaging efficiency of GI remains a key issue to be resolved because a minimum number of measurements are required to construct CGI [3]. Therefore, several methods were proposed to mitigate this issue, and a typical approach used compressed sensing or compressive sampling (CS) [10] to reduce the number of measurements required for image recovery. On the basis of CS, maximum likelihood-style algorithms were developed for Poissonian and approximate Gaussian modeling of random observations, which resulted in an approximative Gaussian distribution with invariant variance results in the algorithm that was efficient for Poissonian observations [11]. Matthew *et al.* [12] proposed an approach that replaced a sensor

with a pixelated transmission mask, which was encoded with a series of binary patterns. Moreover, a time-of-flight 3D camera with structured illumination was used to implement compressed sensing strategy [13], thus minimizing the acquisition time and obtaining a high resolution for light detection and ranging. Adaptive methods, such as multi-scale [14], were proposed to adjust the field of view (FOV) and transverse coherence width of pseudo-thermal field illumination. Another content-adaptive GI [2] was proposed by using spatiotemporal redundancy in natural images, and high reconstruction quality and frame rates of 16 fps with 64×64 pixel resolution were obtained. Jiang *et al.* [3] suggested an adaptive regional single-pixel imaging method without CS to decrease the number of projected patterns and obtain sharp image reconstructions. Inspired by the vertebrate eye, Phillips *et al.* [15] adopted an adaptive foveated sampling method to improve the frame rate of GI, thereby enabling the image reconstruction results to obtain high resolution and effective exposure time in accordance with a scene.

As a special foveated visual system, human retina, with space-variant distribution of photo-sensitive cells, can encode a large FOV with a variable spatial resolution [16], [17]; this capability results in a high resolution in the FOV center and low resolution in the FOV periphery. On the basis of the feature of human retina structure, the relationship between the retina and the visual cortex is subject to an approximate logarithmic-polar law, thereby resulting in fine properties of redundant compression and invariances of scaling and rotation imaging system [18]. These properties improve the imaging efficiency with large FOV. Besides that, the retina-like method is considered a complementary for existing CS methods to further improve the imaging efficiency of GI.

However, the current retina-like image sensors [19], [20] based on space-variant array structure are unsuitable to be applied directly in adaptive GI because the pixel size cannot be changed when the sensor parameters are specified. Alternatively, DMD, the core device of the CGI, can not only reach high frame rates up to 22 kHz but also achieve adaptive sampling because sampling patterns are easily programmable in accordance with different scenes. Moreover, pixel binning strategy enables DMD to adjust the resolution of the spatial sampling structure flexibly. Therefore, applying the retina-like method on the DMD is able to achieve a programmable variable spatial resolution sampling and no additional devices are needed, which is highly suitable for CGI. Additionally, the retina-like structure is also suitable for target recognition and tracking because rotation and scaling invariances are available from log-polar transformation [18].

In summary, retina-like sampling is an emerging and promising approach to CGI. In contrast to the adaptive foveated sampling method that exploits the spatiotemporal redundancy of dynamic scenes [15], retina-like sampling is based on the retino-cortical mapping, thus resulting in fine properties of redundant compression, target recognition and tracking because of the log-polar transformation. To our knowledge, the systematic theoretical studies on retina-like ghost imaging are lacking, especially for three-dimensional imaging. Therefore, the main contribution of this study is proposing a retina-like 3DCGI (R-3DCGI) and developing its models to illustrate the principle and working process. Several simulations are conducted to study the R-3DCGI and find an effective approach to balancing high resolution and imaging efficiency.

2. R-3DCGI 3D Models

The R-3DCGI scheme is illustrated in Fig. 1. A pulsed laser (PL) is triggered by a signal generator (SG). Random speckles are produced by the DMD that is illumined by the PL, which is used to illuminate a target. The one-dimensional time-resolved total intensity distribution of a reflected or scattered light from the target is collected by a time-resolved bucket detector (TBD). The CGI of a certain depth slice (namely at a certain distance) is obtained by a correlated pre-calculated intensity of target from a DMD pattern and TBD intensity of the corresponding time slice [21], as depicted in the right-down part of Fig. 1, where m = 1,2,3,... M (M is the total number of pulses), and n = 1,2,3,... N (N is the maximum number of time slices in accordance with individual pulse). A TBD is used to receive the target intensity at various distances, that is, different depth slices, to obtain 3D GI. In the system, speckle patterns, that is, reference arms, can be precomputed by controlling the
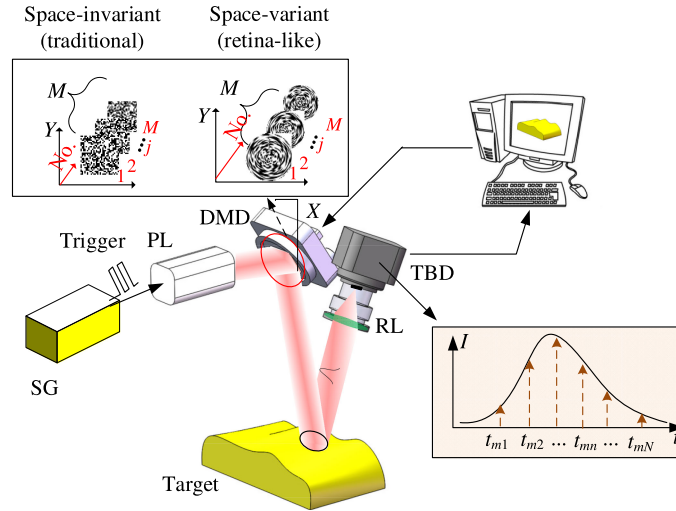
Fig. 1. Principle of the R-3DCGI. SG-signal generator, PL-pulsed laser, DMD- digital micromirror device, RL-receiving lens, TBD-time-resolved bucket detector.

DMD. The resolution of these patterns is space-variant, which is a remarkable difference between the traditional 3DCGI (T-3DCGI) and the proposed method.

We deduce the R-3DCGI models on the basis of Fig. 1 as follows. The 3DCGI can be viewed as a series of tomographic images reconstructed by 2DCGI for given slices [7]; therefore, we obtain

$$G_n\left(\vec{r}\right) = \frac{1}{M}\sum_{m=1}^{M} B_n\left(t_{mn}\right) \cdot R_n\left(\vec{r}, t_{mn} - \frac{t_n}{2}\right) - \frac{1}{M}\sum_{m=1}^{M} B_n\left(t_{mn}\right) \cdot \frac{1}{M}\sum_{m=1}^{M} R_n\left(\vec{r}, t_{mn} - \frac{t_n}{2}\right), \qquad (1)$$

where $G_n(\vec{r})$ is the 3DCGI at an n-to slice($\vec{r}$ means the coordinates on the slice), $B_n(t_{mn})$ is the measurement of the time-resolved bucket at the mn-to time slice of the No.n pulse and $R_n(\vec{r}, t_{mn} - \frac{t_n}{2})$ is the intensity distribution of the corresponding speckle pattern that illuminates the target(t_{mn} is the time-of-light (TOF) between the system and the mn-th depth slice of the target, t_n is the TOF between the system and the n-to slice of the target). Assuming the intensity distribution of the PL is a Gaussian function, which is written as [22]

$$P\left(\vec{r}, t\right) = \frac{P_0}{\tau\sqrt{2\pi}} \cdot exp\left(-\frac{t^2}{2\tau^2}\right) \cdot \frac{2}{\pi W_0^2} \cdot exp\left[-\frac{2\vec{r}^2}{W_0^2}\right], \qquad (2)$$

where P_0 denotes the pulse power, λ is the source wavelength, τ is the pulse width, and W_0 is the waist radius of the laser. Then the intensity distribution through the DMD is expressed as

$$P_s\left(\vec{r}, t\right) = \frac{P_0}{\tau\sqrt{2\pi}} \cdot exp\left(-\frac{t^2}{2\tau^2}\right) \cdot \frac{2}{\pi W_0^2} \cdot exp\left[-\frac{2\vec{r}^2}{W_0^2}\right] \cdot I_s\left(\vec{r}, t\right), \qquad (3)$$

where $I_s(\vec{r}, t)$ is the modulated function of the DMD, which is controlled by a computer. Accordingly, the intensity distribution of the speckle pattern that illuminates the target can be defined as

$$\begin{cases} R_n\left(\vec{r}, t\right) = \frac{P_0}{\tau\sqrt{2\pi}} \cdot exp\left(-\frac{(t-t_n/2)^2}{2\tau^2}\right) \cdot \frac{2}{\pi W(L_n)^2} \cdot exp\left[-\frac{2\vec{r}^2}{W(L_n)^2}\right] \cdot I_s\left(\vec{r} \cdot \frac{W_0}{W(L_n)}, t - t_n/2\right) \\ W\left(L_n\right) = W_0\sqrt{1 + \left(\frac{\lambda c t_n}{2\pi W_0}\right)^2}, \end{cases} \qquad (4)$$
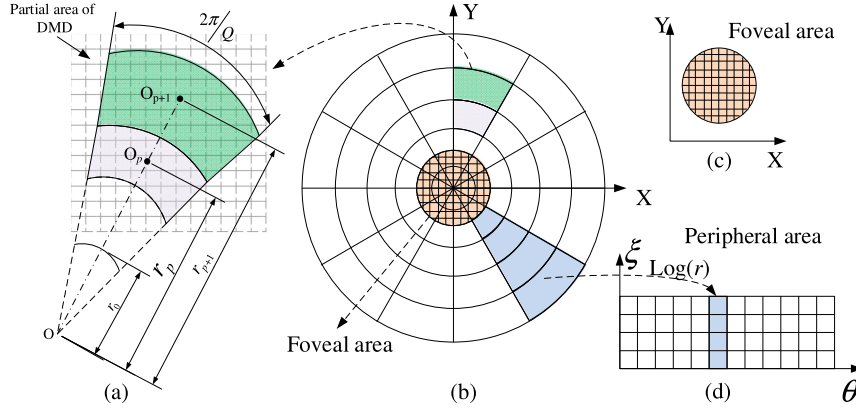
Fig. 2. Retina-like structure on the DMD. (a) Details of the peripheral area of the retina-like structure. (b) Retina-like structure includes the foveal and peripheral areas. (c) Foveal area. (d) Peripheral sampling.

where $W(L_n)$ is the waist radius at n-th depth slice L_n from the DMD. Owing that the total intensity reflected from the target is written as

$$P_{rn}\left(\vec{r}, t\right) = R_n\left(\vec{r}, t\right) \cdot T\left(\vec{r}\right), \tag{5}$$

where $T(\vec{r})$ is the target reflectivity distribution. Hence the pattern of the reflected light (RL) on the plane of the time-resolved bucket detector is expressed as

$$P_{Bn}\left(\vec{r}, t\right) = \frac{P_0}{\tau\sqrt{2\pi}} \cdot exp\left(-\frac{(t - t_n)^2}{2\tau^2}\right) \cdot \frac{2}{\pi W(2L_n)^2} \cdot exp\left[-\frac{2\vec{r}}{W(2L_n)^2}\right]$$
$$\cdot I_s\left(\vec{r} \cdot \frac{W_0}{W(2L_n)}, t - t_n\right) \cdot T\left(\vec{r} \cdot \frac{W(L_n)}{W(2L_n)}\right). \tag{6}$$

And the measurement of the time-resolved bucket detector is defined as

$$B_n(t) = \sum_{\vec{r}} P_{Bn}\left(\vec{r}, t\right). \tag{7}$$

Eq. (7) theoretically describes the T-3DCGI. In contrast to the T-3DCGI, the pixels in the DMD are programmed in accordance with the retina-like structure in the R-3DCGI. The sample mode of each pixel in the DMD depends on the relationship between the distance r from the pixel to the center of the DMD and the radius r_0 of the foveal area. The geometry of the space-variant sampling on the DMD is demonstrated in Fig. 2(a), including P rings. Each ring consists of Q pixels. The samples with high fixed resolution are in the foveal area, whereas those with low resolution are in the peripheral area, as exhibited in Fig. 2(b). The resolution decreases with the increase in eccentricity.

We develop the R-3DCGI on the basis of the space-variant geometry on the DMD as follows. With reference to our previous study on the retina-like structure [23], two parameters, namely, pth radius and degree in q sector, are expressed as

$$\begin{cases} r_{p+1} = r_1 \cdot \varepsilon^p \\ \varepsilon = \frac{1 + \sin(\pi/Q)}{1 - \sin(\pi/Q)} \\ r_1 = \frac{r_0}{1 - \sin(\pi/Q)} \\ \theta_q = q \cdot \frac{2\pi}{Q} \quad (q = 1, 2, 3...Q) \\ \xi_p = \log_\varepsilon(r_p) = \log_\varepsilon(r_1) + p - 1 \quad (p = 1, 2, 3...P), \end{cases} \tag{8}$$

where r_p is the radius of the pth ring, $(1+\sin(\pi/Q))/(1-\sin(\pi/Q))$ is the increasing coefficient ε, and θ_q is the degree of the q sector. Similar to the derivation of the T-3DCGI, the space-variant intensity distribution on the DMD is defined as

$$P_s\left(r_p, \theta_q, t\right) = \frac{P_0}{\tau\sqrt{2\pi}} \cdot \exp\left(-\frac{t^2}{2\tau^2}\right) \cdot \frac{2}{\pi W_0{}^2} \cdot \exp\left[-\frac{2r_p{}^2}{W_0{}^2}\right] \cdot I_s\left(r_p, \theta_q, t\right). \tag{9}$$

The intensity distribution on the target through distance L is written as

$$R_n\left(r_p', \theta_q, t\right) = \frac{P_0}{\tau\sqrt{2\pi}} \cdot \exp\left(-\frac{(t-t_n/2)^2}{2\tau^2}\right) \cdot \frac{2}{\pi W(L_n)^2} \cdot \exp\left(-\frac{2r_p{}'^2}{W(L_n)^2}\right)$$

$$\cdot I_s\left(r_p' \cdot \frac{W_0}{W(L_n)}, \theta_q, t - t_n/2\right), \tag{10}$$

where (r_p', θ_q) is the coordinate on the target. Furthermore, the intensity reflected from the target is expressed as

$$P_{rn}\left(r_p', \theta_q, t\right) = R_n\left(r_p', \theta_q, t\right) \cdot T\left(r_p', \theta_q\right), \tag{11}$$

where $T(r_p', \theta_q)$ is the target reflectance on the retina-like coordinate (r_p', θ_q). The intensity of the RL that focuses on the TBD is

$$P_{Bn}\left(r_p'', \theta_q, t\right) = \frac{P_0}{\tau\sqrt{2\pi}} \cdot \exp\left(-\frac{(t-t_n)^2}{2\tau^2}\right) \cdot \frac{2}{\pi W(2L_n)^2} \cdot \exp\left[-\frac{2r_p{}''^2}{W(2L_n)^2}\right]$$

$$\cdot I_s\left(r_p'' \frac{W_0}{W(2L_n)}, \theta_q, t - t_n\right) \cdot T\left(r_p'' \frac{W(L_n)}{W(2L_n)}, \theta_q\right), \tag{12}$$

where (r_p'', θ_q) is the coordinate on the RL. Therefore, the total intensity of the TBD accumulates all rings and sectors from the retina-like samples, which are defined as

$$B_n'(t) = \sum_{p=1}^{P}\sum_{q=1}^{Q} P_{Bn}\left(r_p'', \theta_q, t\right). \tag{13}$$

We obtain the final intensity of the TBD on the basis of a fixed resolution on the fovea and a space-variant resolution on the periphery by combining Eqs. (7) and (13) as follows:

$$B_n''(t) = B_n'(t) + \int_{\vec{r} \leq r_0 \frac{W(2L)}{W_0}} P_{Bn}\left(\vec{r}, t\right) d\vec{r}. \tag{14}$$

The principle of CGI implies that the target image can be divided into two parts, namely, fovea and peripheral areas. For the fovea area, we obtain

$$G_n\left(\vec{r}\right) = \frac{1}{M}\sum_{m=1}^{M} B_n''(t_{mn}) \cdot R_n\left(\vec{r}, t_{mn} - \frac{t_n}{2}\right) - \frac{1}{M}\sum_{m=1}^{M} B_n''(t_{mn}) \cdot \frac{1}{M}\sum_{m=1}^{M} R_n\left(\vec{r}, t_{mn} - \frac{t_n}{2}\right). \tag{15}$$

For the peripheral area, we realize

$$G_n\left(r_p', \theta_q\right) = \frac{1}{M}\sum_{m=1}^{M} B_n''(t_{mn}) \cdot R_n\left(r_p', \theta_q, t_{mn} - \frac{t_n}{2}\right) - \frac{1}{M}\sum_{m=1}^{M} B_n''(t_{mn}) \cdot \frac{1}{M}\sum_{m=1}^{M} R_n\left(r_p', \theta_q, t_{mn} - \frac{t_n}{2}\right). \tag{16}$$

Eqs. (15) and (16) are the T-3DCGI and R-3DCGI, respectively. A comparison of Eqs. (15) and (16) indicates that $G(r_p', \theta_q)$ is related to different space-invariant p and q.
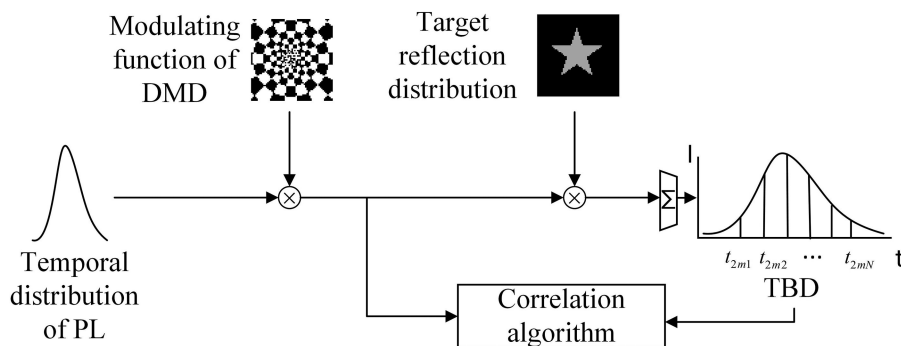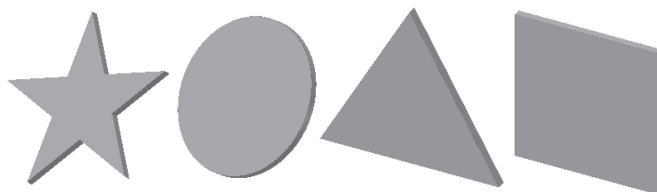
Fig. 3. Setup of the R-3DCGI simulation.

Fig. 4. Geometric models of the targets.

3. Simulations and Results

3.1 Simulation Setup

The processes of the numerical simulations are displayed in Fig. 3. The intensity distribution through the DMD, which is determined by a temporal function of the PL in Eq. (2) and the retina-like structure modulating function of the DMD, is divided into the foveal distribution expressed by Eq. (3) and the peripheral distribution expressed by Eq. (8). The modulating function of the DMD is discretized in 2D lattices by Eq. (8), as presented in Fig. 2. However, the value of each element in the 2D lattices is generated by the Bernoulli distribution and is independent of one another statistically, which similar to the simplified T-3DCGI.

In the simulation setup, the reference intensity distribution and total intensity of the TBD are required to reconstruct 3D images. On the one hand, the reference intensity distribution on the target is computed by the intensity distribution through the DMD, object distance L, and beam radius through L, as expressed in Eqs. (4) and (10). On the other hand, the total intensity of the TBD is described by Eqs. (6) and (7) and (13) and (14). Additionally, we substitute the total intensity of TBD including noise for the total intensity of TBD to simulate the detecting process actually in the simulation process [11]. On the basis of the abovementioned measurements, the 3D images in the foveal and peripheral areas are obtained in accordance with Eqs. (14) and (15), respectively.

For a more realistic R-3DCGI simulation, we consider applying retina-like structure on a real DMD device. The specified DMD we choosing is a Texas Instruments DLP Discovery 4100 development kit. The DLP development kit is equipped with a 0.7-inch DMD, containing 1024×768 micro mirrors. The maximum binary modulation rate of the DMD is 22.7 kHz. And the size of each mirror is 13.6×13.6 μm^2. Combining these physical parameters of the DMD and the retina-like structure modulating function above, the R-3DCGI simulation progress can reconstruct a target in virtual physical scene instead of the simple numerical simulations for principle.

To evaluate the performance of the R-3DCGI, four targets (i.e., a pentagram, a circle, a triangle, and a rectangle) are selected to verify the models, as illustrated in Fig. 4. The corresponding parameters, including size and surface reflectivity, are listed in Table 1. The parameters of the PLs are set as follows: the pulse energy is 1 nJ; the wavelength is 1550 nm; and the initial pulse width and beam radius are 1 ns and 25 mm, respectively. Additionally, for comparison and analysis, the

TABLE 1
Simulation Parameters of the Targets

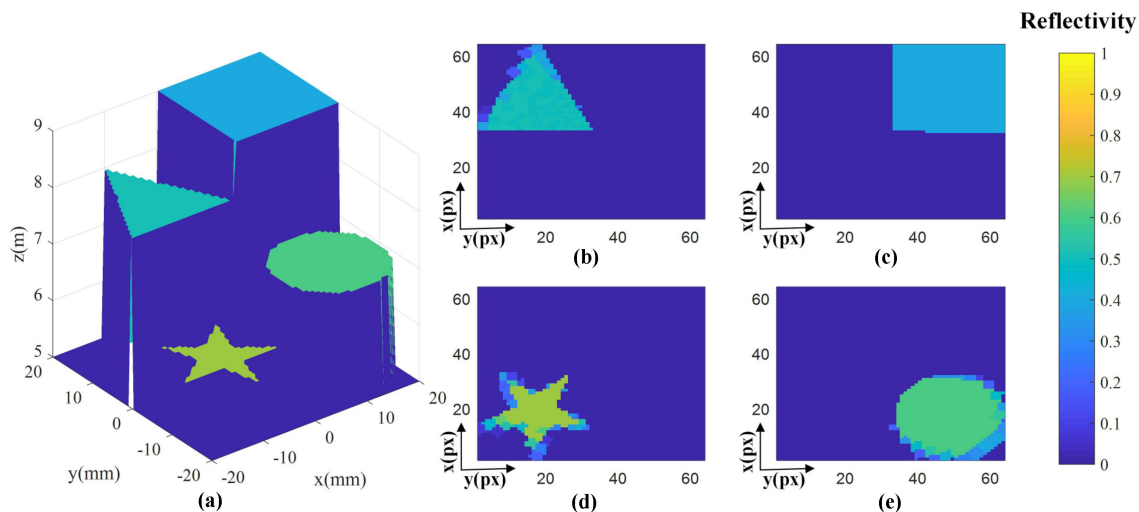| Target	Parameter	Value	Target	Parameter	Value
	Length	7.3 mm		Radius	10 mm
Pentagram	Object distance	6 m	Circle	Object distance	7 m
	Surface reflectivity	0.7		Surface reflectivity	0.6
				Length	20 mm
	Length	20 mm		Width	20 mm
Equilateral triangle	Object distance	8 m	Rectangle	Object distance	9 m
	Surface reflectivity	0.5		Surface reflectivity	0.4

Fig. 5. 3D targets and each slice of the R-3DCGI result of the targets. (a) 3D target image; (b)–(e) CGI results of the object distances of 6, 7, 8, and 9 m.

resolution of the simulation results is normalized to 64×64 pixels. The simulations are executed on an Intel Core i5-7600@3.40 GHz computer with 8 GB of RAM memory and Windows 10 operating system.

3.2 R-3DCGI Modeling Verification

We construct the 3D images of the targets under the conditions that the sampling ratio (the ratio between the number of measurements and the number of total pixels in the reconstructed image) is 0.5, and the rings, sectors, and radius of the foveal area are 40, 60, and 4 mm, correspondingly. The slice positions are determined by the different object distances [7].

The 3D target images and slices of the CGI results of the slice simulation are depicted in Fig. 5, where the value of (X, Y, Z) exhibited in the left describes the reflectivity of the (X, Y) on the x–y object plane that is located at the position with Z meters away from the system. The four targets can be distinguished in accordance with their different shapes and reflectivity in the CGI, as demonstrated in Figs. 5(b)–(e). Hence, the R-3DCGI can be reconstructed accurately through the proposed models.
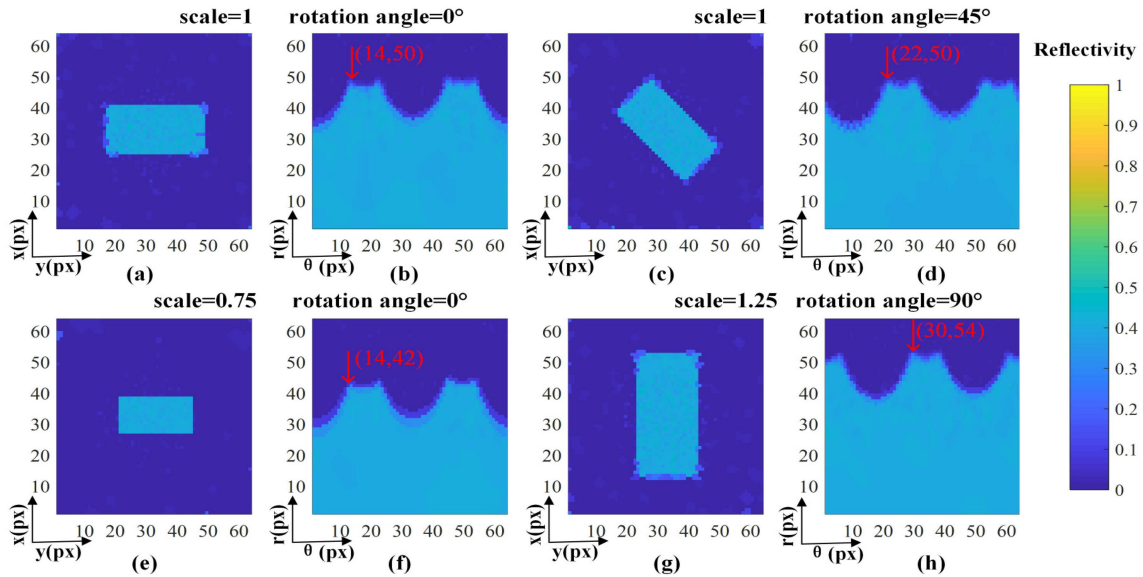
Fig. 6. Reconstructed results of the different groups. The scales and rotation angles of the target are 1 and 0° in (a) and (b), 1 and 45° in (c) and (d), 0.75 and 0° in (e) and (f), and 1.25 and 90° in (g) and (h), correspondingly. The unit is pixel (px).

Furthermore, rotation and scaling invariances, as the main features of the retina-like structure, are tested. Here, we select the rectangle (we set the length scale as 2 times for a highly visible display) to test these features by rotating and scaling the target. In the scaling simulation, the scaling parameter of the target varies from 0.75 to 1.25. In the rotating simulation, the rotation angle is from 0° to 90°. The sampling ratio and parameters of the retina-like structure remain unchanged. Fig. 6 presents the corresponding reconstructed results of different groups in Cartesian coordinates and Log polar coordinates.

Fig. 6 demonstrates the features of the rotation and scaling invariances. Figs. 6(a) and (b) exhibit the reconstructed results of the original target. First, the feature of the rotation invariance is illustrated by comparing Fig. 6(c) and (d), and the rotation angle around the geometrical center of the target in Fig. 6(c) corresponds to the translation along the angle axis in Fig. 6(d). For example, the rotation of a target corresponds to the 8-pixel translation along the θ-axis in Fig. 6(d) when this target rotates 45° around the center in Fig. 6(c) compared with that in Fig. 6(a). Second, the feature of the scaling variance is illustrated by comparing Fig. 6(e) and (f), and the target scale in Fig. 6(e) corresponds to the translation along the log-radius axis in Fig. 6(f). Similarly, the scale of a target corresponds to the 8-pixel translation along the r-axis in Fig. 6(f) when the scale of this target decreases to 0.75 times in Fig. 6(e) compared with that in Fig. 6(a). The scale of a target corresponds to the 4-pixel translation along the r-axis and to the 16-pixel translation along the θ-axis in Fig. 6(h) when the scale of this target increases to 1.25 times and rotates 90° around the center simultaneously in Fig. 6(g), thereby confirming this feature when the rotation angle and scale parameter change simultaneously. Accordingly, the rotation and scaling invariances are verified in the R-3DCGI model.

3.3 Comparative Results

The comparisons for demonstrating the R-3DCGI advantages are divided into the resolution, the compression of the redundant information, time consumption in a single frame reconstruction process and the reconstruction quality of the complex reflectance distribution surface. As for the comparisons of the first three, we select the pentagram in Table 1 as the target and the scale sets to 2 times for a visible display. For fair comparison, R-3DCGI and T-3DCGI are under the same
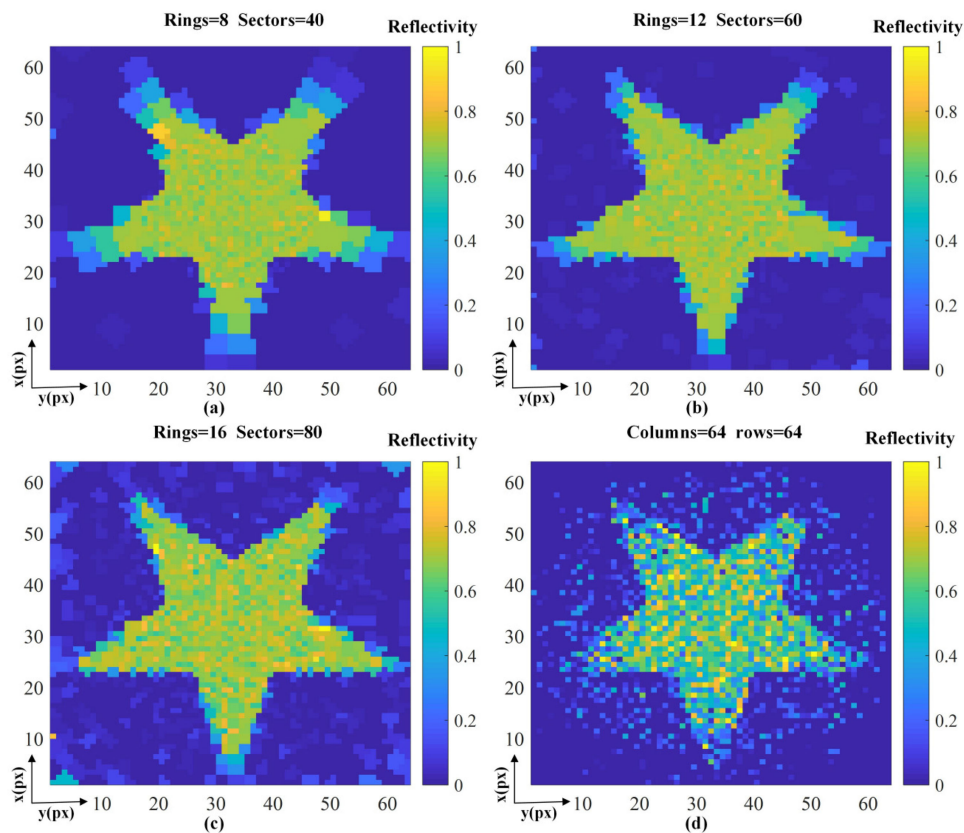
Fig. 7. Comparative reconstruction results of the R-3DCGI and T-3DCGI models. (a)–(c) Results of the R-3DCGI. (d) Result of the T-3DCGI.

TABLE 2

Comparison of the Resolution Between the R-3DCGI and T-3DCGI

Models	Rings × Sectors	Resolution in the fovea	Resolution in the periphery	Total resolution
R-3DCGI	8×40 pixels	621 pixels	320 pixels	941 pixels
R-3DCGI	12×60 pixels	593 pixels	720 pixels	1313 pixels
R-3DCGI	16×80 pixels	593 pixels	1280 pixels	1873 pixels
Models	Columns × Rows			Total resolution
T-3DCGI	64×64 pixels			4096 pixels

FOV [24] and the maximum radius of the imaging area is set to 25 mm. In the R-3DCGI models, the rings and sectors vary from 8×40, 12×60, and 16×80. In the T-3DCGI model, the columns and rows are 64×64. The comparative reconstruction results are displayed in Fig. 7. The radius of the foveal area depends on the parameter value of the rings and sectors of the peripheral area and the maximum radius of the imaging area.

Firstly, comparing the resolution of the R-3DCGI and T-3DCGI, we summarize their resolution characteristics in the Table 2. It is obvious that although the total resolution is lower in the R-3DCGI than in the T-3DCGI, the resolution in the fovea is still high and the resolution in the periphery changes with different rings and sectors in the R-3DCGI. For instance, the total resolution of the

TABLE 3

RRR and RER Values of the R-3DCGI Using Different Rings and Sectors

R-3DCGI (rings × sectors)	RRR	RER
8×40 pixels	0.14	0.86
12×60 pixels	0.31	0.69
16×80 pixels	0.30	0.70

TABLE 4

Comparative Results of the Single Frame Reconstruction Average Time Between the R-3DCGI and T-3DCGI

R-3DCGI (rings × sectors)	Single frame reconstruction time	T-3DCGI (columns × rows)	Single frame reconstruction time
8×40 pixels	0.0670 s		
12×60 pixels	0.1471 s	64×64 pixels	0.3837 s
16×80 pixels	0.2219 s		

R-3DCGI (8×40 pixels) only has 941 pixels far lower than 4096 pixels in the T-3DCGI, but 621 pixels are in the fovea and 320 pixels are in the periphery. Moreover, with the rings and sectors increasing to 12×60 pixels, the resolution in the peripheral area rises to 720 pixels. Additionally, the reconstruction results in Fig. 7 are also accordance with the comparative results and analysis of the resolution visibly.

Next, studying the compression of the redundant information, we introduce two criteria for estimating this feature. We define effective and redundant pixels that describe the pixels of the target and background, and the formulas of relative redundant ratio (RRR) and relative effective ratio (RER) are introduced [25]. RRR is the ratio between the redundant and the entire pixels. Similarly, RER is the ratio between the effective and the total pixels. Combined with Fig. 7, the compression of the redundant information is better based on the R-3DCGI than based on the T-3DCGI. Statistically, the total pixels in Fig. 7(a) are 941 pixels (621 in the fovea and 8×40 in the periphery), and the RRR of the R-3DCGI is 0.14 (131/941). The total pixels of the T-3DCGI are 4096 (64×64), as presented in Fig. 7(d), and the RRR of the T-3DCGI is 0.82 (3358/4096). Therefore, the ratio of the RRR between the R-3DCGI and T-3DCGI will be approximately 1:5.86 (0.14/0.82). The utilization rate of the effective pixels is also better in the R-3DCGI than in the T-3DCGI. In accordance with the definition of the RER, we compare the RER of the two models in Fig. 7(a) and (d). Statistically, the RER of the R-3DCGI is 0.86, whereas the RER of the T-3DCGI is 0.18. Therefore, the RER between the R-3DCGI and T-3DCGI is approximately 4.8:1. Fig. 7(a)–(c) depict the results of the R-3DCGI using different rings and sectors, and their corresponding RRR and RER values are summarized in Table 3.

Then, for the time consumption in a single frame reconstruction process, we record and compare the results of the single frame reconstruction average time between the T-3DCGI and R-3DCGI in Table 4.

Table 4 displays that the R-3DCGI consumes less time than the T-3DCGI in the single frame reconstruction process. For example, the time consumption in the single frame reconstruction average time of the R-3DCGI (8×40 pixels) is 0.0670 s, whereas the time consumption in the T-3DCGI is 0.3837 s. The single frame reconstruction average time also decreases with the rings and sectors.

Lastly, to compare the reconstruction quality for the complex reflectance distribution surface, we choose the circle with the complex reflectance distribution (normalized grey-scale image
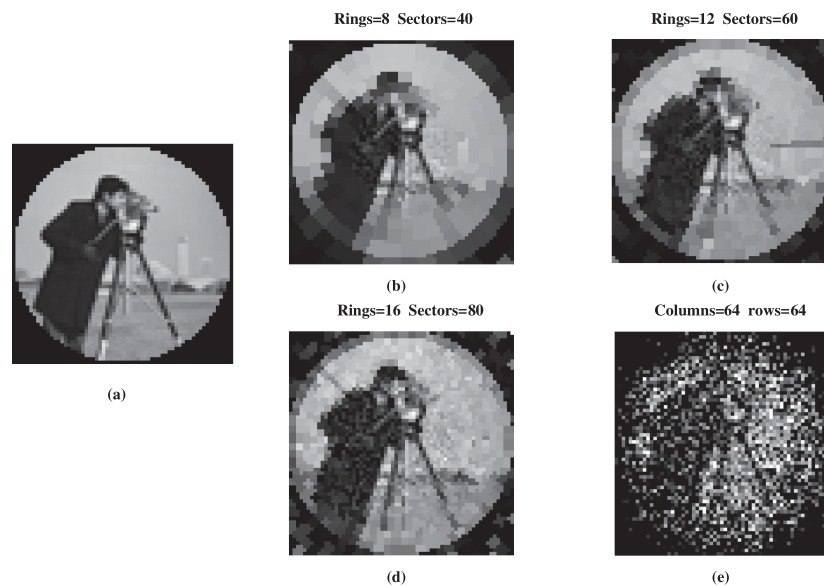
Rings=8 Sectors=40   Rings=12 Sectors=60

(a)

(b)   (c)

Rings=16 Sectors=80   Columns=64 rows=64

(d)   (e)

Fig. 8. Comparative reconstruction results of the R-3DCGI and T-3DCGI models for the complex re-flectance distribution target. (a) The target. (b)–(d) Results of the R-3DCGI. (e) Result of the T-3DCGI.

'cameraman') instead of the simple pentagram and other parameters remain unchanged. The comparative results are shown in Fig. 8.

Fig. 8 shows clearly that the reconstruction quality is much better by R-3DCGI than by T-3DCGI for the complex reflectance distribution target. Moreover, compared among the different R-3DCGI models, the conclusions can be drawn as following: firstly, the local reconstruction quality in the fovea is high fixed, regardless of the rings and the sectors. secondly, with the rings and sectors increasing, both the local reconstruction resolution and noise in the periphery increase.

The comparative results presented above indicate that the R-3DCGI has a variable spatial resolution sampling structure, high compression of the redundant information, low time consumption and different reconstruction quality in different area. Thereby, the R-3DCGI is proved to be able to balance the trade-off between the resolution and imaging efficiency of CGI.

4. Discussions

The features of the R-3DCGI are analyzed. Further discussions on the relationship between signal–noise ratio (SNR) and the retina-like parameters of the R-3DCGI are useful because the favorable structure of the R-3DCGI is beneficial for improving the performances of GI. SNR is defined as $10\lg(G_n/(G_n - G_t))$, the reconstructed target image is G_n and the ground-truth image (namely the reflectivity distribution of the tested object image) is G_t. The rings and sectors (M and N) and the radius of the fovea (r_0), as the main retina-like parameters, are discussed in accordance with Eq. (8).

The rings and sectors vary from 8×40, 12×60, 16×80, and 20×100, similar to those in [26]. We also select the pentagram as the target and set the pentagram scale as 2 times for a highly visible display. For practical use, the maximum radius of the imaging area and the sampling ratio are set to 25 mm and 1, respectively, and other simulation parameters remain unchanged as indicated in Subsection 3.1. Fig. 9(a) presents the trends between the SNR values and the sampling ratio under different rings × sectors of the R-3DCGI. The trend between the SNR values and the R-3DCGI of the same imaging area is illustrated in Fig. 9(a).

The comparison of the different SNR curves of the rings × sectors of the R-3DCGI implies that the SNR tendencies of the R-3DCGI increase fast and then remain steady, but their rising speeds
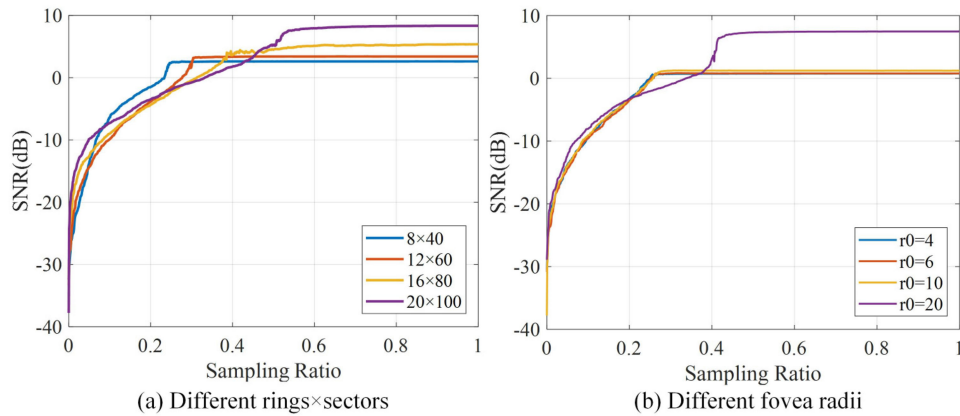
Fig. 9. (a) Relationship between SNR and sampling ratio under different rings × sectors of the R-3DCGI. (b) Relationship between SNR and sampling ratio under different fovea radii.

are different. A few rings and sectors rise to the steady SNR value rapidly because the redundant information decrease with the numbers of rings and sectors, as indicated in Subsection 3.3. The SNR values also increase with the numbers of the rings and sectors considering the increase in the number of pixels, as presented in Subsection 3.3. The SNR values at sampling ratio 1 in the four groups are 2.61, 3.39, 5.36, and 8.33 dB, and the large number corresponds to the large SNR value.

The results in Fig. 9(a) and Table 4 denote that a high SNR is obtained by large rings and sectors, but the single frame reconstruction time is considerable. Therefore, we can adjust the numbers of the rings and sectors to balance the contradiction of SNR and reconstruction time in accordance with the different requirements of the SNR tendency in different situations.

For studying the effect of the fovea radius, the fovea radius varies from 4, 6, and 10 mm to 20 mm. The pentagram of the 2 times scale is still set to the target. The maximum radius of the imaging area, the sectors, and the sampling ratio are set to 25 mm, 60, and 1. The rings can be calculated by using Eq. (8). The other simulation parameters remain unchanged as indicated in Subsection 3.1. Fig. 9(b) depicts the relationship between the SNR curves and the sampling ratio under different fovea radii. The comparison of the different SNR curves of the fovea radius of the R-3DCGI presents that the maximum value of the SNR increases with the increase in the fovea radius given the increased number of pixels. The peak of the maximal values in these SNR curves is 7.47 dB with the fovea radius of 20. By contrast, the nadir of the maximal values in these SNR curves is 0.75 dB with the fovea radius of 4. Similar to the analysis of Fig. 9(a), a large fovea radius leads to a large SNR value and slow increase considering the results in Fig. 9(b) and Table 4. Hence, we must set the proper value of the fovea radius to balance the contradiction of the SNR and the reconstruction time in accordance with the actual situation.

In general, determining the retina-like parameters of the R-3DCGI should be considered synthetically in accordance with the different demands.

5. Conclusions

We propose a R-3DCGI method to obtain high resolution while retaining high imaging efficiency. The corresponding models are deduced, and simulations are conducted to verify the accuracy and features of the models. Several important conclusions are drawn. First, the R-3DCGI has retina-like properties, such as scaling and rotation invariances. Second, the R-3DCGI has higher imaging efficiency than the T-3DCGI with respect to utilizing effective pixels because the R-3DCGI models use the retina-like structure, which is beneficial for improving imaging efficiency. Finally, the

relationships between the SNR and the parameters of the R-3DCGI are discussed to obtain the optimized retina-like structure in different applications.

Acknowledgment

References

[1] B. I. Erkmen and J. H. Shapiro, "Ghost imaging: from quantum to classical to computational," *Adv. Opt. Photon.*, vol. 2, no. 4, pp. 405–450, 2010.
[2] Z. Li, J. Suo, X. Hu, and Q. Dai, "Content-adaptive ghost imaging of dynamic scenes," *Opt. Exp.*, vol. 24, no. 7, pp. 7328–7336, 2016.
[3] H. Jiang, S. Zhu, H. Zhao, B. Xu, and X. Li, "Adaptive regional single-pixel imaging based on the Fourier slice theorem," *Opt. Exp.*, vol. 25, no. 13, pp. 15118–15130, 2017.
[4] H. Yu, E. Li, W. Gong, and S. Han, "Structured image reconstruction for three-dimensional ghost imaging lidar," *Opt. Exp.*, vol. 23, no. 11, pp. 14541–14551, 2015.
[5] M. Bina, D. Magatti, M. Molteni, A. Gatti, L. Lugiato, and F. Ferri, "Backscattering differential ghost imaging in turbid media," *Phys. Rev. Lett.*, vol. 110, no. 8, 2013, Art. no. ,083901.
[6] W.-K. Yu, S. Li, X.-R. Yao, X.-F. Liu, L.-A. Wu, and G.-J. Zhai, "Protocol based on compressed sensing for high-speed authentication and cryptographic key distribution over a multiparty optical network," *Appl. Opt.*, vol. 52, no. 33, pp. 7882–7888, 2013.
[7] W. Gong, C. Zhao, H. Yu, M. Chen, W. Xu, and S. Han, "Three-dimensional ghost imaging lidar via sparsity constraint," *Sci. Rep.*, vol. 6, 2016, Art. no. 26133.
[8] Y. Bai, H. Gao, T. Liu, T. Qiu, and H. Zhou, "Evolution process from ghost diffraction to ghost imaging in a lensless imaging system," *Appl. Opt.*, vol. 50, no. 32, pp. 6098–6102, 2011.
[9] R. E. Meyers, K. S. Deacon, and Y. Shih, "Turbulence-free ghost imaging," *Appl. Phys. Lett.*, vol. 98, no. 11, 2011, Art. no. 111115.
[10] O. Katz, Y. Bromberg, and Y. Silberberg, "Compressive ghost imaging," *Appl. Phys. Lett.*, vol. 95, no. 13, 2009, Art. no. 131110.
[11] V. Katkovnik and J. Astola, "Compressive sensing computational ghost imaging," *JOSA A*, vol. 29, no. 8, pp. 1556–1567, 2012.
[12] M. P. Edgar *et al.*, "Simultaneous real-time visible and infrared video with single-pixel detectors," *Sci. Rep.*, vol. 5, 2015, Art. no. 10669.
[13] M. P. Edgar, M.-J. Sun, G. M. Gibson, G. C. Spalding, D. B. Phillips, and M. J. Padgett, "Real-time 3D video utilizing a compressed sensing time-of-flight single-pixel camera," in *Proc. SPIE*, vol. 9922, Sep. 16, 2016, Art. no. 99221B.
[14] S. Sun *et al.*, "Multi-scale adaptive computational ghost imaging," *Sci. Rep.*, vol. 6, 2016, Art. no. 37013.
[15] D. B. Phillips *et al.*, "Adaptive foveated single-pixel imaging with dynamic supersampling," *Sci. Adv.*, vol. 3, no. 4, 2017, Art. no. e1601782.
[16] J. Najemnik and W. S. Geisler, "Optimal eye movement strategies in visual search," *Nature*, vol. 434, no. 7031, pp. 387–391, 2005.
[17] A. Wannig, L. Stanisor, and P. R. Roelfsema, "Automatic spread of attentional response modulation along Gestalt criteria in primary visual cortex," *Nature Neurosci.*, vol. 14, no. 10, pp. 1243–1244, 2011.
[18] V. J. Traver and A. Bernardino, "A review of log-polar imaging for visual perception in robotics," *Robot. Auton. Syst.*, vol. 58, no. 4, pp. 378–398, 2010.
[19] F. Pardo, B. Dierickx, and D. Scheffer, "Space-variant nonorthogonal structure CMOS image sensor design," *IEEE J. Solid-State Circuits*, vol. 33, no. 6, pp. 842–849, Jun. 1998.
[20] F. Cao, Y. Lin, T. Z. Bai, and F. Wang, "Image rotation-elimination based on a retina-like sensor," *Opt. Eng.*, vol. 54, no. 12, 2015, Art. no. 123105.
[21] Y. Bromberg, O. Katz, and Y. Silberberg, "Ghost imaging with a single detector," *Phys. Rev. A*, vol. 79, no. 5, pp. 1744–1747, 2008.
[22] J. Marques *et al.*, "Temporal and spatial measurements of the electron density perturbation produced in the wake of an ultrashort laser pulse," *Phys. Rev. lett.*, vol. 76, no. 19, pp. 3566–3569, 1996.
[23] J. Cao, Q. Hao, Y. Cheng, F. Zhang, Y. Peng, and H. Yu, "Modeling and simulations on retina-like sensors based on curved surface," *Appl. Opt.*, vol. 55, no. 21, pp. 5738–5744, 2016.
[24] I.-H. Lee, M. T. Mahmood, and T.-S. Choi, "Robust focus measure operator using adaptive log-polar mapping for three-dimensional shape recovery," *Microsc. Microanal.*, vol. 21, no. 2, pp. 442–458, 2015.
[25] J. Cao *et al.*, "Modeling and simulations of three-dimensional laser imaging based on space-variant structure," *Opt. Laser Technol.*, vol. 78, pp. 62–70, 2016.
[26] J. Cao *et al.*, "Design and realization of retina-like three-dimensional imaging based on a MOEMS mirror," *Opt. Lasers Eng.*, vol. 82, pp. 1–13, 2016.